Dear Editor,

We would like to thank you and the reviewer for your constructive comments and suggestions to improve the clarity of our manuscript. We have made changes to address these comments and suggestions.

Point-by-point responses to the comments are provided below. The reviewer comments are in blue, our responses are in red (line numbers refer to those in the revised manuscript), and modifications to the original manuscript are highlighted in yellow.

Please also note that we added an extra author (Pushkar Kopparla) in the second round of revisions. That has not been reflected in the manuscript website.

Vijay Natraj
On behalf of all co-authors

Some of the approved satellite missions (e.g., GHGSAT-D, MethaneSAT) to measure CH_4 are not mentioned while other proposed missions (proposal submitted but not funded or concept published) were mentioned. So you may add some of these on-going missions: GHGSAT-D (McKeever, et al., 2017, AGU Fall Meeting, Varon et al., 2019, GRL), MethaneSAT (Wofsy and Hamburg, 2019, AGU Fall meeting).

We agree with the reviewer and have added the following sentences (lines 76–80).

GHGSat-D (McKeever et al., 2017; Varon et al., 2019; Jervis et al., 2020) measures between 1630–1675 nm, with an effective pixel resolution of $50{\times}50$ m^2 over targeted $12{\times}12$ km^2 scenes, and is intended to detect CH_4 emissions from individual industrial sites. In contrast, MethaneSAT (Wofsy and Hamburg, 2019) has a pixel size of 1–2 km^2 and a wide field of view (200 km^2) and can quantify diffuse CH_4 emission sources over large areas.

Quantifying the impact of aerosol scattering on the retrieval of methane from airborne remote sensing measurements

Yunxia Huang[1,2], Vijay Natraj[3], Zhaocheng Zeng[2,4], Pushkar Kopparla[5], and Yuk L. Yung[2,3]

[1]School of Science, Nantong University, Nantong, 226007, China

[2]Division of Geological and Planetary Sciences, California Institute of Technology, Pasadena, CA 91125, USA

[3]Jet Propulsion Laboratory, California Institute of Technology, Pasadena, CA 91109, USA

[4]Joint Institute for Regional Earth System Science and Engineering, University of California, Los Angeles, CA 90095, USA

[5]Graduate School of Frontier Sciences, The University of Tokyo, Kashiwa, Chiba 277-0882, Japan

Correspondence to: Vijay Natraj (vijay.natraj@jpl.nasa.gov)

Abstract. As a greenhouse gas with strong global warming potential, atmospheric methane (CH_4) emissions have attracted a great deal of attention. Although remote sensing measurements can provide information about CH_4 sources and emissions, accurate retrieval is challenging due to the influence of atmospheric aerosol scattering. In this study, imaging spectroscopic measurements from the Airborne Visible/Infrared Imaging Spectrometer–Next Generation (AVIRIS-NG) in the short-wave infrared are used to compare two retrieval techniques — the traditional Matched Filter (MF) method and the Optimal Estimation (OE) method, which is a popular approach for trace gas retrievals. Using a numerically efficient two-stream-exact-single-scattering radiative transfer model, we also simulate AVIRIS-NG measurements for different scenarios and quantify the impact of aerosol scattering in the two retrieval schemes by including aerosols in the simulations but not in the retrievals. The presence of aerosols causes an underestimation of CH_4 in both the MF and OE retrievals; the biases increase with increasing surface albedo and aerosol optical depth (AOD). Aerosol types with high single scattering albedo and low asymmetry parameter (such as water soluble aerosols) induce large biases in the retrieval. When scattering effects are neglected, the MF method exhibits lower fractional retrieval bias compared to the OE method at high CH_4 concentrations (2–5 times typical background values), and is suitable for detecting strong CH_4 emissions. For an AOD value of 0.3, the fractional biases of the MF retrievals are

34   between 1.3 and 4.5%, while the corresponding values for OE retrievals are in the 2.8–5.6% range. On

35   the other hand, the OE method is an optimal technique for diffuse sources (<1.5 times typical background

36   values), showing up to five times smaller fractional retrieval bias (8.6%) than the MF method (42.6%)

37   for the same AOD scenario. However, when aerosol scattering is significant, the OE method is superior

38   since it provides a means to reduce biases by simultaneously retrieving AOD, surface albedo and CH_4.

39   The results indicate that, while the MF method is good for plume detection, the OE method should be

40   employed to quantify CH_4 concentrations, especially in the presence of aerosol scattering.

1 Introduction

Atmospheric methane (CH_4) is about 85 times more potent per unit mass at warming the Earth than carbon dioxide (CO_2) on a 20-year timescale (IPCC, 2013), implying that reduction in CH_4 emissions could be very efficient to slow down global warming in the near term. Global mean CH_4 concentrations have increased from ~700 ppb in the preindustrial era to more than 1860 ppb as of 2019 (NOAA, 2019). The most effective sink of atmospheric CH_4 is the hydroxyl radical (OH) in the troposphere. CH_4 reacts with OH to reduce the oxidizing capacity of the atmosphere and generate tropospheric ozone. Increasing emissions of CH_4 reduce the concentration of OH in the atmosphere. With less OH to react with, the lifespan of CH_4 could also increase, resulting in greater CH_4 concentrations (Holmes et al., 2013). Soils also act as a major sink for atmospheric methane through the methanotrophic bacteria that reside within them.

Significant natural CH_4 sources include wetlands (Bubier et al., 1994, Macdonald et al., 1998; Gedney et al., 2004), geological seeps (Kvenvolden and Rogers, 2005; Etiope et al., 2009), ruminant animals, and termites. In addition, increased surface and ocean temperatures associated with global warming may increase CH_4 emissions from melting permafrost (Woodwell et al., 1998; Walter et al., 2006; Schaefer et al., 2014, Schuur et al., 2015) and methane hydrate destabilization (Kvenvolden, 1988; Archer, 2007). Human activity also contributes significantly to the total CH_4 emissions. Rice agriculture is one of the most important anthropogenic sources of CH_4 (Herrero et al., 2016; Schaefer et al., 2016). Other sources include landfills (Themelis and Ulloa, 2007), wastewater treatment, biomass burning, and methane slip from gas engines. Global fugitive CH_4 emissions from coal mining (Kort et al., 2014), natural gas and oil systems (Alvarez et al., 2018), hydraulic fracturing ("fracking") of shale gas wells (Howarth et al., 2011; Howarth, 2015, 2019), and residential and commercial natural gas distribution sectors (He et al., 2019) are also of increasing concern. Although the sources and sinks of methane are reasonably well known, there are large uncertainties in their relative amounts and in the partitioning between natural and anthropogenic contributions (Nisbet et al., 2014, 2016). This uncertainty is exemplified by the CH_4 "hiatus", which refers to the observed stabilization of atmospheric CH_4 concentrations from 1999–2006, and the renewed rise thereafter (Kirschke et al., 2013).

Satellite monitoring of CH_4 can be broadly divided into three categories: solar backscatter, thermal emission and lidar (Jacob et al., 2016). The first solar backscattering mission was SCIAMACHY (Frankenberg et al., 2006), which was operational from 2003–2012 and observed the entire planet once every seven days. It was followed by GOSAT in 2009 (Kuze et al., 2016), and subsequently the next generation GOSAT-2 in 2018 (Glumb et al., 2014). In between, the TROPOMI mission was also launched in 2017, which observes the planet once daily with a high spatial resolution of 7×7 km^2 (Butz

74   et al., 2012; Veefkind et al., 2012). CarbonSat (Buchwitz et al., 2013) is another proposed mission to

75   measure CH_4 globally from solar backscatter with a very fine spatial resolution (2×2 km^2) and high

76   precision (0.4%). GHGSat-D (McKeever et al., 2017; Varon et al., 2019; Jervis et al., 2020) measures

77   between 1630–1675 nm, with an effective pixel resolution of 50×50 m^2 over targeted 12×12 km^2 scenes,

78   and is intended to detect CH_4 emissions from individual industrial sites. In contrast, MethaneSAT (Wofsy

79   and Hamburg, 2019) has a pixel size of 1–2 km^2 and a wide field of view (200 km^2) and can quantify

80   diffuse CH_4 emission sources over large areas. Thermal infrared observations of CH_4 are available from

81   the IMG (Clerbaux et al., 2003), AIRS (Xiong et al., 2008), TES (Worden et al., 2012), IASI (Xiong et

82   al., 2013), and CrIS (Gambacorta et al., 2016) instruments. These instruments provide day/night

83   measurements at spatial resolutions ranging from 5×8 km^2 (TES) to 45×45 km^2 (AIRS). GEO-CAPE

84   (Fishman et al., 2012), GeoFTS (Xi et al., 2015), G3E (Butz et al., 2015), and GeoCarb (Polonsky et al.,

85   2014) are proposed geostationary instruments (GeoCarb was selected by NASA under the Earth Venture

86   - Mission program), which when operational will have resolutions of 2–5 km over regional scales. The

87   MERLIN lidar instrument (Kiemle et al., 2014) scheduled for launch in 2021 will measure CH_4 by

88   employing a differential absorption lidar.

89   By combining a large number of footprints and high spatial resolution, airborne imaging

90   spectrometers are also well suited for mapping local CH_4 plumes. The Airborne Visible/Infrared Imaging

91   Spectrometer–Next Generation (AVIRIS-NG) measures reflected solar radiance across more than 400

92   channels between 380 and 2500 nm (Green et al., 1998; Thompson et al., 2015). Strong CH_4 absorption

93   features present between 2100 and 2500 nm can be observed at a spectral resolution of 5 nm full width

94   at half maximum (FWHM). A number of approaches have been developed to retrieve CH_4 from such

95   hyperspectral data. Roberts et al. (2010) used a spectral residual approach between 2000 and 2500 nm

96   and Bradley et al. (2011) employed a band ratio technique using the 2298 nm CH_4 absorption band and

97   2058 nm CO_2 absorption band. However, these techniques are not suited for terrestrial locations that

98   have lower albedos and have spectral structure in the SWIR. A cluster-tuned matched filter technique

99   was demonstrated to be capable of mapping CH_4 plumes from marine and terrestrial sources (Thorpe et

100   al., 2013) as well as CO_2 from power plants (Dennison et al., 2013); however, this method does not

101   directly quantify gas concentrations. Frankenberg et al. (2005) developed an iterative maximum *a*

102   *posteriori* differential optical absorption spectroscopy (IMAP-DOAS) algorithm that allows for

103   uncertainty estimation. Thorpe et al. (2014) adapted the IMAP-DOAS algorithm for gas detection in

104   AVIRIS imagery. In addition, they developed a hybrid approach using singular value decomposition and

105   IMAP-DOAS as a complementary method of quantifying gas concentrations within complex AVIRIS

106   scenes.

107   Accurate assessment of CH_4 emissions is particularly challenging in the presence of aerosols

108   because the latter introduce uncertainties in the light path if not accounted for. In fact, CH_4 emissions are

109   frequently correlated with pollution due to concurrent aerosol emissions. For large aerosols (such as dust),

110   the low Ångström exponent values result in high aerosol optical depth (AOD) values even in the

111   wavelength range from 2000 nm to 2500 nm (Seinfeld and Pandis, 2006; Zhang et al., 2015). Therefore,

112   it is important to obtain a clear understanding of aerosol impacts on CH_4 retrievals. In this study, SWIR

113   AVIRIS-NG measurements are used to analyze the impact of aerosol scattering on CH_4 retrievals.

114   Further, using an accurate but numerically efficient radiative transfer (RT) model (Spurr and Natraj,

115   2011), we simulate AVIRIS-NG measurements with varying aerosol amounts and quantify the impact of

116   aerosol scattering using two retrieval techniques, the traditional matched filter (MF) method and the

117   optimal estimation (OE) method that is widely used in trace gas remote sensing. This article is organized

118   as follows. The MF and OE retrieval methods are described in Section 2. Section 3 focuses on analysis

119   of a sample CH_4 plume detected by AVIRIS-NG measurements and compares retrievals using the MF

120   and OE methods. Section 4 presents a detailed evaluation of aerosol impacts on the two retrieval methods

121   through simulations of AVIRIS-NG spectra for different geophysical parameters. Section 5 provides a

122   summary of the work and discusses future research.

123

124   **2 Methods**

125   **2.1 MF method**

126   Real-time remote detection using AVIRIS-NG measurements are traditionally based on the MF

127   method (Frankenberg et al., 2016). In this method, the background spectra are assumed to be distributed

128   as a multivariate Gaussian $\mathcal{N}$ with covariance matrix $\boldsymbol{\Sigma}$ and background mean radiance $\boldsymbol{\mu}$. If H_0 is a

129   scenario without CH_4 enhancement and H_1 is one with CH_4 enhancement, the MF approach is equivalent

130   to a hypothesis test between the two scenarios:

131    $$H_0: L_{\mathrm{m}} \sim \mathcal{N}(\boldsymbol{\mu}, \boldsymbol{\Sigma}) \tag{1}$$

132    $$H_1: L_{\mathrm{m}} \sim \mathcal{N}(\boldsymbol{\mu} + \boldsymbol{t}\alpha, \boldsymbol{\Sigma}) \tag{2}$$

133   where L_{m} is the measurement radiance; $\boldsymbol{t}$ is the target signature, which is defined in Equation (4); α is the

134   enhancement value, denoting a scaling factor for the target signature that perturbs the background $\boldsymbol{\mu}$. If

135    $\boldsymbol{x}$ is a vector of measurement spectra with one element per wavelength, $\alpha(\boldsymbol{x})$ can be written, based on

136   maximum likelihood estimates (Manolakis et al., 2014), as follows:

137    $$\alpha(\boldsymbol{x}) = \frac{(\boldsymbol{x} - \boldsymbol{\mu})^T \boldsymbol{\Sigma}^{-1} \boldsymbol{t}}{\boldsymbol{t}^T \boldsymbol{\Sigma}^{-1} \boldsymbol{t}} \tag{3}$$

138 We utilize the same definitions as in Frankenberg et al. (2016). Specifically, the enhancement value $\alpha(x)$

139 denotes the thickness and concentration within a volume of equivalent absorption, and has units of ppm

140 × m. The target signature t refers to the derivative of the change in measured radiance with respect to a

141 change in absorption path length due to an optically thin absorbing layer of CH4. Note that this definition

142 has the disadvantage that the accuracy of the result degrades when the absorption is strong and further

143 attenuation becomes nonlinear. At a particular wavelength λ, t can be expressed as:

144
$$t(\lambda) = -\kappa(\lambda)\mu(\lambda), \tag{4}$$

145 where κ is the absorption coefficient for a near-surface plume with units of $\text{ppm}^{-1}\,\text{m}^{-1}$. This is

146 different from the units of $\text{m}^2 \cdot \text{mol}^{-1}$ traditionally used for the absorption coefficient κ_{trad} in trace

147 gas remote sensing. Using the ideal gas law to express the volume V (in liters) occupied by one mole of

148 CH4 at the temperature and pressure corresponding to the plume altitude (V = 22.4 at standard

149 temperature and pressure), and the relations 1 liter = $10^{-3}\,\text{m}^3$ and 1 ppm = 10^{-6}, we obtain the

150 following expression for unit conversion (units in parentheses):

151
$$\kappa_{trad}\,[\text{m}^2 \cdot \text{mol}^{-1}] = \kappa\,[\text{ppm}^{-1}\text{m}^{-1}] \times V\,[\text{liter mol}^{-1}] \times 10^{-3}\,[\text{m}^3\,\text{liter}^{-1}] / 10^{-6}\,[\text{ppm}^{-1}] \tag{5}$$

152 Figure 1 shows the target signature, which is calculated based on HITRAN absorption cross-sections

153 (Rothman et al., 2009). The background mean radiance μ used in Equation 4 is based on the AVIRIS-

154 NG measurement shown in Figure 2; this is described in more detail in Section 3.

155 **2.2 OE method**

156   The OE method is widely used for the remote sensing retrieval of satellite measurements, such as

157 from the Orbiting Carbon Observatory-2 (OCO-2; O'Dell et al., 2018), the Spinning Enhanced Visible

158 and Infra-Red Imager (SEVIRI; Merchant et al., 2013), and the Greenhouse Gases Observing Satellite

159 (GOSAT; Yoshida et al., 2013). It combines an explicit (typically nonlinear) forward model of the

160 atmospheric state, a (typically Gaussian) prior probability distribution for the variabilities and a (typically

161 Gaussian) distribution for the spectral measurement errors. In addition, the Bayesian framework used by

162 the OE approach allows new information (from measurements) to be combined with existing information

163 (e.g., from models). In many applications, the forward model is nonlinear, and obtaining the optimal

164 solution requires iterative techniques such as the Levenberg–Marquardt method (Rodgers, 2000), which

165 has been routinely applied to study the impacts of measurement parameters on the retrieval process (see,

166 e.g., Zhang et al., 2015). The iteration in this algorithm follows the below procedure.

167
$$\mathbf{x}_{i+1} = \mathbf{x}_i + [(1+\gamma)\mathbf{S}_a^{-1} + \mathbf{K}_i^T\mathbf{S}_\epsilon^{-1}\mathbf{K}_i]^{-1}\{\mathbf{K}_i^T\mathbf{S}_\epsilon^{-1}[\mathbf{y} - \mathbf{F}(\mathbf{x}_i)] - \mathbf{S}_a^{-1}[\mathbf{x}_i - \mathbf{x}_a]\} \tag{6}$$

168 where $\mathbf{x}$ is a state vector of surface and atmospheric properties, $\mathbf{S}_a$ is the *a priori* covariance matrix, $\mathbf{S}_\epsilon$

169 is the spectral radiance noise covariance matrix, $\mathbf{K}$ is the Jacobian matrix, $\mathbf{x}_a$ is the *a priori* state vector

170 and γ is a parameter determining the size of each iteration step. The measured spectral radiance is denoted

171   as $\mathbf{y}$; $\mathbf{F}(\mathbf{x})$ is the simulated radiance obtained from the forward model. For the retrieval of CH_4 from

172   AVIRIS-NG measurements, the state vector includes the total column amounts of CH_4 and H_2O, while

173   for the retrievals from synthetic spectra, the H_2O concentration is fixed and the state vector only includes

174   the CH_4 total column. The *a priori* values are within 10% of the true values; *a priori* errors are assumed

175   to be 20% for all state vector elements. The retrieved results are shown as the column averaged mixing

176   ratio (XCH_4, in ppm). Aerosols are not included in the state vector for both the real and synthetic

177   retrievals. They are, however, considered in the forward model for the synthetic simulations. Table 1

178   (WCRP, 1986) lists optical properties for four basic aerosol types (dust, water soluble, oceanic and soot).

179   Table 2 (WCRP, 1986) shows the corresponding properties for three aerosol models that are defined as

180   mixtures of the basic components from Table 1. We employ the Henyey-Greenstein phase function

181   (Henyey and Greenstein, 1941), where aerosol composition is determined by two parameters: single

182   scattering albedo (SSA) and asymmetry parameter (g). The surface albedo is also not retrieved; for both

183   real and synthetic retrievals, it is held fixed and assumed to be independent of wavelength.

184

185   **3 Detection and retrieval of CH_4 from AVIRIS-NG measurements**

186   To illustrate the OE retrieval and its difference from the MF method, we perform retrievals for an

187   AVIRIS-NG measurement made on 4 September 2014 (ang20140904t204546) in Bakersfield, CA, as

188   shown in Figure 2. The location is to the west of the Kern Front Oil field. This detection is a case study

189   from the NASA/ESA CO_2 and MEthane eXperiment (COMEX) campaign in California during June and

190   August/September 2014, which includes airborne *in situ*, airborne non-imaging remote sensing, and

191   ground-based *in situ* instruments to provide a real-time remote detection and measurement for CH_4

192   plumes released from anthropogenic sources. An RGB image of flight data is displayed in Figure 2a; the

193   emission source is a pump jack, as described in Thompson et al. (2015). Figure 2b presents results from

194   the MF method, which shows that the CH_4 plume disperses downwind and has a maximum enhancement

195   value of about 2800 ppm × m. Some artifacts caused by surfaces with strong absorption in the 2100–

196   2500 nm wavelength range, such as oil-based paints or roofs with calcite as a component (Thorpe et al.,

197   2013), also produce large α values in the MF method; these can be removed by an optimization method

198   such as the column-wise MF technique (Thompson et al., 2015).

199   Figure 3 displays the measured radiance (a) before normalization and (b) after normalization,

200   corresponding to two detector elements (in plume and out of plume). Every element is a cross-track

201   spatial location. The normalization is done by calculating the ratio of the radiance to the maximum value

202   across the spectral range, such that the values fall between 0 and 1. This is a first order correction for the

203   effects of surface albedo. Comparing the measured spectrum in plume to that out of plume, there is

204 obvious enhancement of CH_4 that is particularly evident in the normalized radiance. CH_4 is the main

205 absorber in the 2100–2500 nm wavelength range, and H_2O is the major interfering gas. Figure 3b

206 indicates the absorption peaks due to H_2O and CH_4.

207   We choose the plume center with 500 elements to illustrate results obtained using the MF and OE

208 methods. The former evaluates the CH_4 α value compared to the background CH_4 concentration, while

209 the latter retrieves XCH_4. In the MF method, the background covariance matrix Σ and mean radiance

210 μ are drawn from a reference region close to the CH_4 emission source. These are shown in Figure 2,

211 where the dashed green box denotes the reference region and the source is located within the solid red

212 box. In the OE method, results are shown as a multiplicative scaling factor compared to a typical XCH_4

213 background of 1.822 ppm. This value is the globally averaged marine surface annual mean for 2014 (Ed

214 Dlugokencky, NOAA/GML, www.esrl.noaa.gov/gmd/ccgg/trends_ch4/), the year corresponding to the

215 AVIRIS-NG measurement being studied. We use an accurate and numerically efficient two-stream-

216 exact-single-scattering (2S-ESS) RT model (Spurr and Natraj, 2011). This forward model is different

217 from a typical two-stream model in that the two-stream approximation is used only to calculate the

218 contribution of multiple scattering to the radiation field. Single scattering is treated in a numerically exact

219 manner using all moments of the phase function. This model has been used for remote sensing of

220 greenhouse gases and aerosols (Xi et al., 2015; Zhang et al., 2015, 2016; Zeng et al., 2017, 2018).

221 Aerosols are neither included in the forward model nor retrieved in this analysis. The surface albedo is

222 set to a wavelength-independent value of 0.5.

223   Results from the two retrieval methods reveal a similar CH_4 plume shape (Figure 4), especially for

224 elements with high CH_4 enhancement. However, larger differences in CH_4 concentrations are evident in

225 the OE retrievals (Figure 4b). Since radiance normalization reduces the impact of surface albedo and

226 aerosols are not included in either retrieval, this might be due to the fact that, in the OE method, H_2O and

227 CH_4 are simultaneously retrieved; the CH_4 retrieval has added uncertainty due to overlapping absorption

228 features between these two gases. The large maximum value of about 3000 in the MF method also

229 contributes to a reduction in relative contrast. While these results provide heuristic information about the

230 relative performance of the two retrieval techniques, it is difficult to compare the CH_4 enhancement

231 directly between the two methods since the background CH_4 concentration used in the MF method cannot

232 be quantified exactly. Further, evaluating retrieval biases due to ignoring aerosol scattering is not trivial

233 when real measurements are used. Therefore, we simulate synthetic spectra (see section 4) using the 2S-

234 ESS RT model to study the impacts of aerosol scattering as a function of different geophysical parameters

235 by varying them in a systematic manner.

236

237   **4 Aerosol impact analysis**

238   **4.1 Synthetic spectra**

239   In a real AVIRIS-NG observation, the exact column concentration of CH_4 cannot be controlled.

240   However, synthetic simulations allow us to manipulate parameters such as CH_4 concentration, surface

241   albedo, AOD, g, and SSA, and thereby test aerosol impacts on CH_4 retrievals. The 2S-ESS RT model is

242   used to simulate the AVIRIS-NG spectral radiance. In this model, a prior atmospheric profile with 70

243   layers from the surface up to 70 km is derived from National Center for Environmental Prediction

244   reanalysis data (Kalnay et al., 1996); absorption coefficients for all relevant gases are obtained from the

245   HITRAN database (Rothman et al., 2009). Monochromatic RT calculations are performed at a spectral

246   resolution of 0.5 cm^{-1}; the radiance spectrum is then convolved using a Gaussian instrument line shape

247   function with a wavelength-dependent full width at half maximum (FWHM) from a calibrated AVIRIS-

248   NG data file. The signal to noise ratio (SNR) is set to be 300, with Gaussian white noise added. This

249   procedure results in a wavelength grid with a resolution of about 5 nm. The spectral wavelength range

250   used to retrieve CH_4 is from 2100 nm to 2500 nm.

251   The additional atmospheric and geometric variables included in the model are listed in Table 3,

252   which are held constant unless otherwise mentioned. The observation geometry parameters are taken

253   from a real AVIRIS-NG measurement. Recent AVIRIS-NG fight campaigns have sensor heights ranging

254   from 0.43 to 3.8 km; we choose a value of 1 km, the same as the highest level where aerosol is present

255   in our simulations. The influence of AOD on CH_4 retrieval as a function of SSA and g is analyzed in

256   Section 4.3; in all other cases, SSA and g are held constant at 0.95 and 0.75, respectively, which is

257   representative of aerosols in the Los Angeles region (Zhang et al., 2015).

258   **4.2 Aerosol impact in the MF method**

259   We simulate synthetic spectra at different AOD, surface albedo and CH_4 concentration values, use

260   the MF method to obtain the CH_4 enhancement, and compare differences in α between scenarios without

261   and with aerosol. The covariance matrix and background mean radiance are calculated from a simulated

262   zero AOD background with surface albedos from 0.1 to 0.5, and XCH_4 set at the typical background

263   value of 1.822 ppm used in Section 3. Figure 5a shows the enhancement value as a function of XCH_4.

264   As the CH_4 concentration increases, the enhancement value obtained by the MF method at first increases

265   approximately linearly. However, the absorption changes in a nonlinear fashion with concentration,

266   whereas the MF method applies a linear formalism to the change. Therefore, the enhancement value

267   (which is correlated with the absorption signature) also shows a deviation from linear behavior at larger

268   XCH_4. Two aerosol scenarios (AOD = 0, 0.3) are compared in Figure 5a, which reveals that the effect of

269   aerosol loading is similar to an underestimation of CH_4 in the retrieval. The underestimation, which is

270   due to the shielding of CH_4 absorption below the aerosol layer and the fact that multiple scattering effects

271   between the aerosol and the surface are ignored, is clearly shown in Figure 5b, where the enhancement

272   value for fixed CH_4 concentration (same concentration as the background) decreases from 0 ppm × m

273   to −1532 ppm × m with increasing AOD. To clarify the impact of AOD at different surface albedo values,

274   zoomed in versions of α as a function of XCH_4 are presented in Figures 5c–f. For the AOD = 0 scenario,

275   the results are independent of surface albedo. This is because there are no multiple scattering effects

276   between the surface and the atmosphere (Rayleigh scattering is negligible in the retrieval wavelength

277   range) when there is no aerosol loading. For the scenarios with aerosol loading, the dispersion in the

278   zero-enhancement XCH_4 value between different surface albedos indicates that results from the MF

279   method are biased more at large AOD and surface albedo values (Figures 5d–f). This is a consequence

280   of increased multiple scattering between the aerosol layer and the surface that is not accounted for by the

281   retrieval algorithm. The maximum bias value is close to − 700 ppm × m (equivalent to − 0.06 × 1.822

282   ppm relative to the background concentration of 1.0 × 1.822 ppm) for an AOD of 0.3 and surface albedo

283   of 0.5 (Figure 5f). The implication of these results is that accurate knowledge of the surface albedo is

284   important for MF retrievals, especially when the aerosol loading is large.

285   A quantitative analysis of underestimation of CH_4 concentration due to aerosol scattering is

286   presented in Figure 6. The color bar shows the α bias — which is defined as the difference between the

287   enhancement value without aerosol (true α value) and that with aerosol — for different CH_4

288   concentrations, surface albedos and AODs. A positive bias means that CH_4 is underestimated. The α bias

289   increases with increasing surface albedo and AOD, reaching a maximum value of about 700 ppm × m

290   for the simulated cases. However, it is interesting that the bias decreases with increasing CH_4

291   concentration, which is different from the results obtained by the OE method (discussed in Section 4.3).

292   This surprising behavior is a direct consequence of the physical basis of the MF method. The rate of

293   increase in enhancement becomes smaller as XCH_4 becomes larger (Figure 5a). Therefore, at higher

294   XCH_4 values, the addition of aerosols (which has a similar effect as a reduction in XCH_4) results in a

295   lower reduction in enhancement compared to that at lower XCH_4 values, resulting in a net decrease in

296   the enhancement bias.

297   **4.3 Aerosol impact in the OE method**

298   For the simulation of the synthetic spectra, we assume nonzero aerosol loading below 1 km elevation.

299   The OE method is then used to perform retrievals using the same configuration (including, in particular,

300   the same surface albedo) except that AOD is set to zero. This approach is similar to neglecting aerosol

301   scattering in the CH_4 retrieval; the retrieval bias is defined as the difference between the true XCH_4 in

302   the simulation and the retrieved value (positive values refer to underestimation). First, we study the

10

303 retrieval bias caused by different aerosol types and mixtures. Figure 7a shows CH_4 retrieval biases as a

304 function of SSA and g; surface albedo and AOD are kept constant at 0.3 and XCH_4 is assumed to be 1.0

305 × 1.822 ppm. The retrieval bias increases with SSA and decreases with g, with a maximum bias ratio

306 (ratio of retrieval bias to the true value) of about 20%. This behavior can be explained as follows. At

307 higher SSA values, there are more multiple scattering effects (that are ignored in the retrieval). On the

308 other hand, larger values of g imply greater anisotropy of scattering (preference for forward scattering),

309 leading to a reduction in multiple scattering effects. Since the retrieval bias is large for high SSA and

310 low g, the water-soluble aerosol type (Table 1) and the maritime aerosol model (Table 2) can be expected

311 to induce greater biases in the retrieval. In order to compare the impacts of SSA and g in further detail,

312 retrieval results due to a ± 5% change in SSA and g for the three aerosol models from Table 2 are shown

313 in Figures 7b and 7c. Note that for the maritime aerosol model, the SSA is set to 0.999 for the +5%

314 scenario to ensure physicality. It is clear that (1) the maritime aerosol model induces larger retrieval

315 biases than the other aerosol types, and (2) the retrieval results are more sensitive to changes in g than

316 those in SSA.

317   We then simulate synthetic spectra for different values of CH_4 concentration, surface albedo and

318 AOD. The impacts of aerosol scattering on the retrievals for these scenarios are demonstrated in Figure

319 8. Figure 8a shows a 5 × 5 panel of boxes. Within each box, XCH_4 is constant, while surface albedo

320 increases from top to bottom and AOD increases from left to right. The variation of XCH_4 across the

321 boxes is shown in Figure 8b. We also show a zoomed in plot of the bottom right box ($XCH_4 = 5.8 \times$

322 1.822 ppm) in Figure 8c, which illustrates the AOD and surface albedo changes within a box. These

323 changes are identical for all boxes. Figure 8a indicates that OE retrievals produce larger CH_4 biases at

324 higher XCH_4 values, in contrast with MF results. In addition, it is evident that the retrieved CH_4 bias

325 increases with increasing AOD. The CH_4 bias induced by differences in the surface albedo is not as large

326 as that due to AOD variations, but surface albedo effects are noticeable at large AOD. Figure 8d shows

327 the sensitivity of retrieval biases to changes in AOD and surface albedo, again demonstrating the greater

328 impact of AOD than surface albedo in the retrieval.

329   The effects of changing the *a priori*, *a priori* error and RT simulation spectral resolution on the

330 retrieved XCH_4 are shown in Figure 9. For these calculations, the other parameters are set as follows:

331 SSA = 0.95, g = 0.75, AOD = 1.0, surface albedo = 0.5 and true $XCH_4 = 5.8 \times 1.822$ ppm. The parameters

332 were chosen to correspond to the scenario with the largest retrieval bias in Figure 8c (bottom right box

333 in Figure 8c). Figure 9a shows that the retrieved XCH_4 changes by about 9 ppb as the *a priori* changes

334 from half to twice the true XCH_4 value. Similarly, the XCH_4 difference is less than 4 ppb when the *a*

335 *priori* error changes from 0.05 to 0.5 (Figure 9b). Compared to the bias of about 923 ppb induced by

336   neglecting aerosol scattering for this scenario, it is clear that the impacts of the *a priori* and *a priori* error

337   are very small. The effect of spectral resolution is larger, but XCH$_4$ still changes by only about 100 ppb

338   when the spectral resolution is changed from 0.5 to 0.1 cm^{-1} (Figure 9c).

339   **4.4 Comparison of the two retrieval techniques**

340   Figure 10 presents the bias ratios for the two retrieval techniques at different AODs (surface albedo

341   = 0.3). In the MF method, the bias ratio is defined as the ratio of the bias to the true value of α. On the

342   other hand, in the OE method, it is the ratio of the bias to the true XCH$_4$. From Figure 10 it is clear that

343   the bias ratio decreases with increasing CH$_4$ concentration and has higher values at larger AODs. The

344   bias ratio for the MF method (1.3–4.5%) is up to 53.6% less than that for the OE method (2.8–5.6%) for

345   AOD = 0.3 when the CH$_4$ concentration is high (2–5 times typical background values). On the other

346   hand, the OE method performs better when enhancements are small and XCH$_4$ is close to the background

347   value. For example, the bias ratio for the MF method has a high value of about 42.6% at AOD = 0.3 for

348   a 10% enhancement (XCH$_4$ = 1.1 × 1.822 ppm); the OE value for the same scenario is 8.6%. For scenarios

349   where scattering is ignored, the two retrieval techniques seem to be complementary, with differing

350   utilities for different enhancements. On the other hand, when RT models that account for scattering

351   effects are employed, the MF technique is suboptimal. Further, MF retrievals rely on accurate

352   characterization of the surface albedo, especially when the aerosol loading is large. Finally, the MF

353   method does not retrieve concentrations, which are necessary to infer fluxes. Therefore, the OE technique

354   is in general superior due to its ability to support simultaneous retrieval of aerosols, surface albedo and

355   CH$_4$ concentration.

356

357   **5 Summary and discussion**

358   Remote sensing measurements from airborne and satellite instruments are widely used to detect

359   CH$_4$ emissions. In our study, the traditional MF and the OE methods are used to quantify the effects of

360   aerosol scattering on CH$_4$ retrievals based on simulations of AVIRIS-NG measurements. The results

361   show that the retrieval biases increase with increasing AOD and surface albedo for both techniques. In

362   the OE method the biases increase with increasing CH$_4$ concentration and SSA, but decrease with

363   increasing aerosol asymmetry parameter. The CH$_4$ retrieval bias increases with increasing XCH$_4$ in the

364   OE method but decreases for the same scenario in the MF method. The surprising MF trend is attributed

365   to the inability of the MF method to treat nonlinear absorption effects at high XCH$_4$ values. We also

366   present bias ratios for the two techniques. The MF method shows smaller bias ratios at large CH$_4$

367   concentrations than the OE method; it is, therefore, the optimal method to detect strong CH$_4$ emission

368   sources when scattering effects can be ignored in the retrieval. For the same retrieval scenario, the OE

369 method seems to be more suitable for detecting diffuse sources. Further, the MF method relies on a

370 comparison with the background CH_4 concentration. It is difficult to get an accurate estimate of the

371 background XCH_4 value in polluted atmospheric environments. In contrast, the OE method provides

372 retrievals based solely on the atmospheric scenario of interest; CH_4, aerosols and surface albedo can be

373 simultaneously inferred. Therefore, when scattering effects need to be considered, the OE method is the

374 appropriate choice. Indeed, the MF method was intended for plume detection. OE enables accurate

375 quantification of XCH_4 in the presence of aerosol scattering.

376   This study focused on a comparison of retrieval techniques. It is also important to accurately

377 represent the physics of atmospheric RT, especially for scenarios with significant aerosol scattering. RT

378 models traditionally used in retrievals of imaging spectroscopic data use simplified radiation schemes

379 and predefined aerosol models, which may introduce inaccurate in the representation of atmospheric

380 physics. The 2S-ESS model provides the capability to quantify aerosol impacts on CH_4 retrieval for

381 different aerosol types, optical depths and layer heights. In future work, we will compare retrievals using

382 the 2S-ESS model against those from other commonly used models such as MODTRAN. We will also

383 evaluate the impact of varying instrument spectral resolution and signal to noise ratio for simultaneous

384 retrieval of CH_4, surface albedo and AOD. This will be relevant for the design of imaging spectrometers

385 for planned future missions such as the NASA Surface Biology and Geology (SBG) mission.

386

387 **Data availability**

388   The code and data are available from the authors upon request.

389

390 **Author contributions**

391   VN conceived the work, provided the radiative transfer and aerosol models, supervised YH, and

392 assisted with manuscript preparation. YH designed and performed the retrievals, analyzed the results,

393 and prepared the original manuscript. ZZ contributed to retrieval setup and assisted with analysis of the

394 results. PK provided valuable inputs into the science of CH_4 remote sensing. YLY supervised YH and

395 participated in the evaluation of the retrieval results and intercomparison. All listed authors contributed

396 to the review and editing of this manuscript.

397

398 **Competing interests**

399   The authors declare that they have no conflict of interest.

400

401 **Acknowledgements**

13

415   **References**

416

417   Alvarez, R. A., Zavala-Araiza, D., Lyon, D. R., Allen, D. T., Barkley, Z. R., Brandt, A. R., Davis, K. J.,

418   Herndon, S. C., Jacob, D. J., Karion, A., Kort, E. A., Lamb, B. K., Lauvaux, T., Maasakkers, J. D.,

419   Marchese, A. J., Omara, M., Pacala, S. W., Peischl, J., Robinson, A. L., Shepson, P. B., Sweeney, C.,

420   Townsend-Small, A., Wofsy, S. C., and Hamburg, S. P.: Assessment of methane emissions from the U.S.

421   oil and gas supply chain, Science, 361, 186–188, https://doi.org/10.1126/science.aar7204, 2018.

422

423   Archer, D.: Methane hydrate stability and anthropogenic climate change, Biogeosci., 4, 521–544,

424   https://doi.org/10.5194/bg-4-521-2007, 2007.

425

426   Bradley, E. S., Leifer, I., Roberts, D. A., Dennison, P. E., and Washburn, L.: Detection of marine methane

427   emissions   with   AVIRIS   band   ratios,   Geophys.   Res.   Lett.,   38,   L10702,

428   https://doi.org/10.1029/2011GL046729, 2011.

429

430   Bubier, J. L., and Moore, T. R: An ecological perspective on methane emissions from northern wetlands,

431   Trends in Ecology and Evolution, 9, 460–464, https://doi.org/10.1016/0169-5347(94)90309-3, 1994.

432

433   Buchwitz, M., Reuter, M., Bovensmann, H., Pillai, D., Heymann, J., Schneising, O., Rozanov, V., Krings,

434   T., Burrows, J. P., Boesch, H., Gerbig, C., Meijer, Y., and Löscher, A.: Carbon Monitoring Satellite

435   (CarbonSat): Assessment of atmospheric CO_2 and CH_4 retrieval errors by error parameterization, Atmos.

436   Meas. Tech., 6, 3477–3500, https://doi.org/10.5194/amt-6-3477-2013, 2013.

437

438   Butz, A., Galli, A., Hasekamp, O., Landgraf, J., Tol, P., and Aben, I.: TROPOMI aboard Sentinel-5

439   Precursor: Prospective performance of CH_4 retrievals for aerosol and cirrus loaded atmospheres, Remote

440   Sens. Environ., 120, 267–276, https://doi.org/10.1016/j.rse.2011.05.030, 2012.

441

442   Butz, A., Orphal, J., Checa-Garcia, R., Friedl-Vallon, F., von Clarmann, T., Bovensmann, H., Hasekamp,

443   O., Landgraf, J., Knigge, T., Weise, D., Sqalli-Houssini, O., and Kemper, D.: Geostationary Emission

444   Explorer for Europe (G3E): Mission concept and initial performance assessment, Atmos. Meas. Tech., 8,

445   4719–4734, https://doi.org/10.5194/amt-8-4719-2015, 2015.

446

15

447 Clerbaux, C., Hadji-Lazaro, J., Turquety, S., Mégie, G., and Coheur, P.-F.: Trace gas measurements from
448 infrared satellite for chemistry and climate applications, Atmos. Chem. Phys., 3, 1495–1508,
449 https://doi.org/10.5194/acp-3-1495-2003, 2003.

450

451 Dennison, P. E., Thorpe, A. K., Pardyjak, E. R., Roberts, D. A., Qi, Y., Green, R. O., Bradley, E. S., and
452 Funk, C. C.: High spatial resolution mapping of elevated atmospheric carbon dioxide using airborne
453 imaging spectroscopy: Radiative transfer modeling and power plant plume detection, Remote Sens.
454 Environ., 139, 116-129, https://doi.org/10.1016/j.rse.2013.08.001, 2013.

455

456 Etiope, G., Feyzullayev, A., and Baciu, C. L.: Terrestrial methane seeps and mud volcanoes: A global
457 perspective of gas origin, Mar. Pet. Geol., 26, 333–344, https://doi.org/10.1016/j.marpetgeo.2008.03.001,
458 2009.

459

460 Fishman, J. L., Iraci, L. T., Al-Saadi, J., Chance, K., Chavez, F., Chin, M., Coble, P., Davis, C.,
461 DiGiacomo, P. M., Edwards, D., Eldering, A., Goes, J., Herman, J., Hu, C., Jacob, D. J., Jordan, C., Kawa,
462 S. R., Key, R., Liu, X., Lohrenz, S., Mannino, A., Natraj, V., Neil, D., Neu, J., Newchurch, M., Pickering,
463 K., Salisbury, J., Sosik, H., Subramaniam, A., Tzortziou, M.,Wang, J., and Wang, M.: The United States'
464 next generation of atmospheric composition and coastal ecosystem measurements: NASA's
465 Geostationary Coastal and Air Pollution Events (GEO-CAPE) Mission, Bull. Am. Meteorol. Soc.,
466 https://doi.org/10.1175/BAMS-D-11-00201.1, 2012.

467

468 Frankenberg, C., Platt, U., and Wagner, T.: Iterative maximum a posteriori (IMAP)-DOAS for retrieval
469 of strongly absorbing trace gases: Model studies for CH_4 and CO_2 retrieval from near infrared spectra of
470 SCIAMACHY onboard ENVISAT, Atmos. Chem. Phys., 5, 9–22, https://doi.org/10.5194/acp-5-9-2005,
471 2005.

472

473 Frankenberg, C., Meirink, J. F., Bergamaschi, P., Goede, A., P. H., Heimann, M., Körner, S., Platt, U.,
474 van Weele, M., and Wagner, T.: Satellite chartography of atmospheric methane from SCIAMACHY on
475 board ENVISAT: Analysis of the years 2003 and 2004, J. Geophys. Res., 111, D07303,
476 https://doi.org/10.1029/2005JD006235, 2006.

477

478 Frankenberg, C., Thorpe, A. K., Thompson, D. R., Hulley, G., Kort, E. A., Vance, N., Borchardt, J.,
479 Krings, T., Gerilowski, K., Sweeney, C., Conley, S., Bue, B. D., Aubrey, A. D., Hook, S., and Green, R.

480   O.: Airborne methane remote measurements reveal heavy-tail flux distribution in Four Corners region,

481   Proc. Natl. Acad. Sci. U. S. A., 113, 9734–9739, https://doi.org/10.1073/pnas.1605617113, 2016.

482

483   Gambacorta, A., Barnet, C. D., Smith, N., Pierce, R. B., Smith, J. W., Spackman, J. R., and Goldberg,

484   M.: The NPP and J1 NOAA Unique Combined Atmospheric Processing System (NUCAPS) for

485   atmospheric thermal sounding: Recent algorithm enhancements tailored to near real time users

486   applications, Abstract IN33D-07, presented at 2016 Fall Meeting, AGU, San Francisco, CA, 12–16 Dec.,

487   2016.

488

489   Gedney, N., Cox, P. M., and Huntingford, C.: Climate feedback from wetland methane emissions,

490   Geophys. Res. Lett., 31, L20503. https://doi.org/10.1029/2004GL020919, 2004.

491

492   Glumb, R., Davis, G., and Lietzke, C.: The TANSO-FTS-2 instrument for the GOSAT-2 greenhouse gas

493   monitoring mission, 2014 IEEE Geoscience and Remote Sensing Symposium, Quebec City, QC, 1238–

494   1240, https://doi.org/10.1109/IGARSS.2014.6946656, 2014.

495

496   Green, R. O., Eastwood, M. L., Sarture, C. M., Chrien, T. G., Aronsson, M., Chippendale, B. J., Faust,

497   J. A., Pavri, B. E., Chovit, C. J., Solis, M., Olah, M. R., and Williams, O.: Imaging spectroscopy and the

498   Airborne Visible/Infrared Imaging Spectrometer (AVIRIS), Remote Sens. Environ., 65, 227–248,

499   https://doi.org/10.1016/S0034-4257(98)00064-9, 1998.

500

501   He, L., Zeng, Z.-C., Pongetti, T. J., Wong, C., Liang, J., Gurney, K. R., Newman, S., Yadav, V., Verhulst,

502   K., Miller, C. E., and Duren, R.: Atmospheric methane emissions correlate with natural gas consumption

503   from residential and commercial sectors in Los Angeles, Geophys. Res. Lett., 46, 8563–8571,

504   https://doi.org/10.1029/2019GL083400, 2019.

505

506   Henyey, L. G., and Greenstein, J. L.: Diffuse radiation in the galaxy, Astrophys. J., 93, 70–83,

507   https://doi.org/10.1086/144246, 1941.

508

509   Herrero, M., Henderson, B., Havlík, P., Thornton, P. K., Conant, R. T., Smith, P., Wirsenius, S., Hristov,

510   A. N., Gerber, P., Gill, M., Butterbach-Bahl, K., Valin, H., Garnett, T., and Shehfest, E.: Greenhouse gas

511   mitigation potentials in the livestock sector, Nature Clim. Change, 6, 452–461,

512   https://doi.org/10.1038/nclimate2925, 2016.

513

514 Holmes, C. D., Prather, M. J., Søvde, O. A., and Myhre, G.: Future methane, hydroxyl, and their

515 uncertainties: key climate and emission parameters for future predictions, Atmos. Chem. Phys., 13, 285–

516 302, https://doi.org/10.5194/acp-13-285-2013, 2013.

517

518 Howarth, R. W.: Methane emissions and climatic warming risk from hydraulic fracturing and shale gas

519 development: implications for policy, Energy and Emission Control Technologies, 3, 45–54,

520 https://doi.org/10.2147/EECT.S61539, 2015.

521

522 Howarth, R. W.: Ideas and perspectives: is shale gas a major driver of recent increase in global

523 atmospheric methane?, Biogeosciences, 16, 3033–3046, https://doi.org/10.5194/bg-16-3033-2019, 2019.

524

525 Howarth, R. W., Santoro, R., and Ingraffea, A.: Methane and the greenhouse gas footprint of natural gas

526 from shale formations, Clim. Change, 106, 679, https://doi.org/10.1007/s10584-011-0061-5, 2011.

527

528 Jacob, D. J., Turner, A. J., Maasakkers, J. D., Sheng, J., Sun, K., Liu, X., Chance, K., Aben, I., McKeever,

529 J., and Frankenberg, C.: Satellite observations of atmospheric methane and their value for quantifying

530 methane emissions, Atmos. Chem. Phys., 16, 14371–14396, https://doi.org/10.5194/acp-16-14371-2016,

531 2016.

532

533 Jervis, D., McKeever, J., Durak, B. O. A., Sloan, J. J., Gains, D., Varon, D. J., Ramier, A., Strupler, M.,

534 and Tarrant, E.: The GHGSat-D imaging spectrometer, Atmos. Meas. Tech. Discuss.,

535 https://doi.org/10.5194/amt-2020-301, in review, 2020.

536

537 Kalnay, E., Kanamitsu, M., Kistler, R., Collins, W., Deaven, D., Gandin, L., Iredell, M., Saha, S., White,

538 G., Woollen, J., Zhu, Y., Chelliah, M., Ebisuzaki, W., Higgins, W., Janowiak, J., Mo, K. C., Ropelewski,

539 C., Wang, J., Leetmaa, A., Reynolds, R., Jenne, R., and Joseph, D.: The NCEP/NCAR 40-year reanalysis

540 project, Bull. Am. Meteorol. Soc., 77, 437–471, https://doi.org/10.1175/1520-

541 0477(1996)077<0437:TNYRP>2.0.CO;2, 1996.

542

543 Kiemle, C., Kawa, S. R., Quatrevalet, M., and Browell, E. V.: Performance simulations for a spaceborne

544 methane lidar mission, J. Geophys. Res., 119, 4365–4379, https://doi.org/10.1002/2013JD021253, 2014.

545

546 Kirschke, S., Bousquet, P., Ciais, P., Saunois, M., Canadell, Josep G., Dlugokencky. E. J., Bergamaschi,

547 P., Bergmann, D., Blake, D. R., Bruhwiler, L., Cameron-Smith, P., Castaldi, S., Chevallier, F., Feng, L.,

548 Fraser, A., Heimann, M, Hodson, E. L., Houweling, S., Josse, B., Fraser, P. J., Krummel, P. B., Lamarque,

549 J.-F., Langenfelds, R. L., Le Quere, C., Naik, V., O'Doherty, S., Palmer, P. I., Pison, I., Plummer, D.,

550 Poulter, B., Prinn, R. G., Rigby, M., Ringeval, B., Santini, M. Schmidt, M., Shindell, D. T., Simpson, I.

551 J., Spahni, R., Steele, L. P., Strode, S. A., Sudo, K., Szopa, S., van der Werf, G. R., Voulgarakis, A., van

552 Weele, M., Weiss, R. F., Williams, J. E., and Zeng, G.: Three decades of global methane sources and

553 sinks, Nature Geosci., 6, 813–823, https://doi.org/10.1038/ngeo1955, 2013.

554

555 Kort, E. A., Frankenberg, C., Costigan, K. R., Lindenmaier, R., Dubey, M. K., and Wunch, D.: Four

556 corners: the largest US methane anomaly viewed from space, Geophys. Res. Lett., 41, 6898–6903,

557 https://doi.org/10.1002/2014GL061503, 2014.

558

559 Kuze, A., Suto, H., Shiomi, K., Kawakami, S., Tanaka, M., Ueda, Y., Deguchi, A., Yoshida, J., Yamamoto,

560 Y., Kataoka, F., Taylor, T. E., and Buijs, H. L.: Update on GOSAT TANSO-FTS performance, operations,

561 and data products after more than 6 years in space, Atmos. Meas. Tech., 9, 2445–2461,

562 https://doi.org/10.5194/amt-9-2445-2016, 2016.

563

564 Kvenvolden, K. A.: Methane hydrate – A major reservoir of carbon in the shallow geosphere, Chem.

565 Geol., 71, 41–51, https://doi.org/10.1016/0009-2541(88)90104-0, 1988.

566

567 Kvenvolden, K. A., and Rogers, B. W.: Gaia's breath – global methane exhalations, Mar. Pet. Geol., 22,

568 579–590, https://doi.org/10.1016/j.marpetgeo.2004.08.004, 2005.

569

570 Macdonald, J. A., Fowler, D., Hargreaves, K. J., Skiba, U., Leith, I. D., and Murray, M. B.: Methane

571 emission rates from a northern wetland; response to temperature, water table and transport, Atmos.

572 Environ., 32, 3219–3227, https://doi.org/10.1016/S1352-2310(97)00464-0, 1998.

573

574 Manolakis, D., Truslow, E., Pieper, M., Cooley, T., and Brueggeman, M.: Detection algorithms in

575 hyperspectral imaging systems: An overview of practical algorithms, IEEE Signal Proc. Mag., 31, 24–

576 33, https://doi.org/10.1109/MSP.2013.2278915, 2014.

577

578 McKeever, J., Durak, B. O. A., Gains, D., Varon, D. J., Germain, S., and Sloan, J. J.: GHGSat-D:
579 Greenhouse gas plume imaging and quantification from space using a Fabry-Perot imaging spectrometer,
580 Abstract A33G-1360 presented at 2017 Fall Meeting, AGU, New Orleans, LA, 11–15 December, 2017.

582 Merchant, C. J., Le Borgne, P., Roquet, H., and Legendre, G.: Extended optimal estimation techniques
583 for sea surface temperature from the Spinning Enhanced Visible and Infra-Red Imager (SEVIRI),
584 Remote Sens. Environ., 131, 287–297, https://doi.org/10.1016/j.rse.2012.12.019, 2013.

586 Myhre, G., Shindell, D., Bréon, F.-M., Collins, W., Fuglestvedt, J., Huang, J., Koch, D., Lamarque, J.-
587 F., Lee, D., Mendoza, B., Nakajima, T., Robock, A., Stephens, G., Takemura, T., and Zhang, H.:
588 Anthropogenic and Natural Radiative Forcing, Climate Change 2013: The Physical Science Basis.
589 Contribution of Working Group I to the Fifth Assessment Report of the Intergovernmental Panel on
590 Climate Change – IPCC, 2013.

592 Nisbet, E. G., Dlugokencky, E, J., and Bousquet, P.: Methane on the rise-Again, Science, 343, 493–495,
593 https//doi.org/10.1126/science.1247828, 2014.

595 Nisbet, E. G., Dlugokencky, E. J., Manning, M. R., Lowry, D., Fisher, R. E., France, J. L., Michel, S. E.,
596 Miller, J. B., White, J. W. C., Vaughn, B., Bousquet, P., Pyle, J. A., Warwick, N. J., Cain, M., Brownlow,
597 R., Zazzeri, G., Lanoisellé, M., Manning, A. C., Gloor, E., Worthy, D. E. J., Brunke, E.-G., Labuschagne,
598 C., Wolff, E. W., and Ganesan, A. L.: Rising atmospheric methane: 2007–2014 growth and isotopic shift,
599 Glob. Biogeochem. Cycles, 30, 1356–1370, https://doi.org/10.1002/2016GB005406, 2016.

601 NOAA Earth System Research Laboratory Global Monitoring Laboratory,
602 https://esrl.noaa.gov/gmd/ccgg/trends_ch4/, 2019.

604 O'Dell, C. W., Eldering, A., Wennberg, P. O., Crisp, D., Gunson, M. R., Fisher, B., Frankenberg, C.,
605 Kiel, M., Lindqvist, H., Mandrake, L., Merrelli, A., Natraj, V., Nelson, R. R., Osterman, G. B., Payne,
606 V. H., Taylor, T. E., Wunch, D., Drouin, B. J., Oyafuso, F., Chang, A., McDuffie, J., Smyth, M., Baker,
607 D. F., Basu, S., Chevallier, F., Crowell, S. M. R., Feng, L., Palmer, P. I., Dubey, M., García, O. E.,
608 Griffith, D. W. T., Hase, F., Iraci, L. T., Kivi, R., Morino, I., Notholt, J., Ohyama, H., Petri, C., Roehl,
609 C. M., Sha, M. K., Strong, K., Sussmann, R., Te, Y., Uchino, O. and Velazco, V. A.: Improved retrievals

610   of carbon dioxide from Orbiting Carbon Observatory-2 with the version 8 ACOS algorithm, Atmos.

611   Meas. Tech., 11(12), 6539–6576, https://doi.org/10.5194/amt-11-6539-2018, 2018.

612

613   Polonsky, I. N., O'Brien, D. M., Kumer, J. B., O'Dell, C. W., and the geoCARB Team: Performance of

614   a geostationary mission, geoCARB, to measure CO_2, CH_4 and CO column-averaged concentrations,

615   Atmos. Meas. Tech., 7, 959–981, https://doi.org/10.5194/amt-7-959-2014, 2014.

616

617   Roberts, D. A., Bradley, E. S., Cheung, R., Leifer, I., Dennison, P. E., and Margolis, J. S.: Mapping

618   methane emissions from a marine geological seep source using imaging spectrometry, Remote Sens.

619   Environ., 114, 592–606, https://doi.org/10.1016/j.rse.2009.10.015, 2010.

620

621   Rodgers, C. D.: Inverse Methods for Atmospheric Sounding: Theory and Practice, World Scientific,

622   Singapore, 2000.

623

624   Rothman, L. S., Gordon, I. E., Barbe, A., Benner, D. C., Bernath, P. E., Birk, M., Boudon, V., Brown,

625   L. R., Campargue, A., Champion, J. P., Chance, K., Coudert, L. H., Dana, V., Devi, V. M., Fally, S.,

626   Flaud, J. M., Gamache, R. R., Goldman, A., Jacquemart, D., Kleiner, I., Lacome, N., Lafferty, W. J.,

627   Mandin, J. Y., Massie, S. T., Mikhailenko, S. N., Miller, C. E., Moazzen-Ahmadi, N., Naumenko, O. V.,

628   Nikitin, A. V., Orphal, J., Perevalov, V. I., Perrin, A., Predoi-Cross, A., Rinsland, C. P., Rotger, M.,

629   Šimečková, M., Smith, M. A. H., Sung, K., Tashkun, S. A., Tennyson, J., Toth, R. A., Vandaele, A. C.,

630   and Vander Auwera, J.: The HITRAN 2008 molecular spectroscopic database, J. Quant. Spectrosc.

631   Radiat. Transfer, 110, 533–572, https://doi.org/10.1016/j.jqsrt.2009.02.013, 2009.

632

633   Schaefer, H., Fletcher, S. E. M., Veidt, C., Lassey, K. R., Brailsford, G. W., Bromley, T. M.,

634   Dlugokencky, E. J., Michel, S. E., Miller, J. M., Levin, I., Lowe, D. C., Martin, R. J., Vaughn, B. H., and

635   White, J. W. C.: A 21st-century shift from fossil-fuel to biogenic methane emissions indicated by $^{13}CH_4$,

636   Science, 352, 80-84, https://doi.org/10.1126/science.aad2705, 2016.

637

638   Schaefer, K., Lantuit, H., Romanovsky, V. E., Schuur, E. A. G., and Witt, R.: The impact of the

639   permafrost carbon feedback on global climate, Environ. Res. Lett., 9, 085003,

640   https://doi.org/10.1088/1748-9326/9/8/085003, 2014.

641

642   Schuur, E. A. G., McGuire, A. D., Schädel, C., Grosse, G., Harden, J. W., Hayes, D. J., Hugelius, G.,

643   Koven, C. D., Kuhry, P., Lawrence, D. M., Natali, S. M., Olefeldt, D., Romanovsky, V. E., Schaefer, K.,

644   Turetsky, M. R., Treat, C. C., and Vonk, J. E.: Climate change and the permafrost carbon feedback,

645   Nature, 520, 171–179, https://doi.org/10.1038/nature14338, 2015.

646

647   Seinfeld, J. H., and Pandis, S. N.: Atmospheric Chemistry and Physics: From Air Pollution to Climate

648   Change, Wiley, New Jersey, USA, 2006.

649

650   Spurr, R., and Natraj, V.: A linearized two-stream radiative transfer code for fast approximation of

651   multiple-scatter fields, J. Quant. Spectrosc. Radiat. Transfer, 112, 2630–2637,

652   https://doi.org/10.1016/j.jqsrt.2011.06.014, 2011.

653

654   Themelis, N. J., and Ulloa, P. A.: Methane generation in landfills, Renewable Energy, 32, 1243–1257,

655   https://doi.org/10.1016/j.renene.2006.04.020, 2007.

656

657   Thompson, D. R., Leifer, I., Bovensmann, H., Eastwood, M., Fladeland, M., Frankenberg, C.,

658   Gerilowski, K., Green, R. O., Kratwurst, S., Krings, T., Luna, B., and Thorpe, A. K.: Real-time remote

659   detection and measurement for airborne imaging spectroscopy: a case study with methane, Atmos. Meas.

660   Tech., 8, 4383–4397, https://doi.org/10.5194/amt-8-4383-2015, 2015.

661

662   Thorpe, A. K., Frankenberg, C., and Roberts, D. A.: Retrieval techniques for airborne imaging of

663   methane concentrations using high spatial and moderate spectral resolution: Application to AVIRIS,

664   Atmos. Meas. Tech., 7, 491–506, https://doi.org/10.5194/amt-7-491-2014, 2014.

665   Thorpe, A. K., Roberts, D. A., Bradley, E. S., Funk, C. C., Dennison, P. E., and Leifer, I.: High resolution

666   mapping of methane emissions from marine and terrestrial sources using a Cluster-Tuned Matched Filter

667   technique and imaging spectrometry, Remote Sens. Environ., 134, 305–318,

668   https://doi.org/10.1016/j.rse.2013.03.018, 2013.

669

670   Varon, D. J., McKeever, J., Jervis, D., Maasakkers, J. D., Pandey, S., Houweling, S., Aben, I., Scarpelli,

671   T. and Jacob, D. J.: Satellite discovery of anomalously large methane point sources from oil/gas

672   production, Geophys. Res. Lett., 2019.

673

674   Veefkind, J. P., Aben, I., McMullan, K., Forster, H., de Vries, J.,Otter, G., Claas, J., Eskes, H. J., de Haan,

675   J. F., Kleipool, Q., van Weele, M., Hasekamp, O., Hoogeveen, R., Landgraf, J., Snel, R., Tol, P., Ingmann,

676   P., Voors, R., Kruizinga, B., Vink, R., Visser, H., and Levelt, P. F.: TROPOMI on the ESA Sentinel-5

677   Precursor: A GMES mission for global observations of the atmospheric composition for climate, air

678   quality and ozone layer applications, Remote Sens. Environ., 120, 70–83,

679   https://doi.org/10.1016/j.rse.2011.09.027, 2012.

680

681   Walter, K. M., Zimov, S. A., Chanton, J. P., Verbyla, D., and Chapin III, F. S.: Methane bubbling from

682   Siberian thaw lakes as a positive feedback to climate warming, Nature, 443, 71–75,

683   https://doi.org/10.1038/nature05040, 2006.

684

685   Wofsy, S. C., and Hamburg, S: MethaneSAT — A new observing platform for high resolution

686   measurements of methane and carbon dioxide, Abstract A53F-02 presented at 2019 Fall Meeting, AGU,

687   San Francisco, CA, 9–13 December, 2019.

688

689   World Climate Research Program (WCRP): A preliminary cloudless standard atmosphere for radiation

690   computation, International Association for Meteorology and Atmospheric Physics, Radiation

691   Commission, Boulder, CO, USA, 1984, CSP-112, WMO/TD-No. 24, March 1986.

692

693   Woodwell, G. M., Mackenzie, F. T., Houghton, R. A., Apps, M., Gorham, E., and Davidson, E.: Biotic

694   feedbacks in the warming of the earth, Climatic Change, 40, 495–518,

695   https://doi.org/10.1023/A:1005345429236, 1998.

696

697   Worden, J., Kulawik, S., Frankenberg, C., Payne, V., Bowman, K., Cady-Peirara, K., Wecht, K., Lee, J.-

698   E., and Noone, D.: Profiles of CH_4, HDO, H_2O, and N_2O with improved lower tropospheric vertical

699   resolution from Aura TES radiances, Atmos. Meas. Tech., 5, 397–411, https://doi.org/10.5194/amt-5-

700   397-2012, 2012.

701

702   Xi, X., Natraj, V., Shia, R. L., Luo, M., Zhang, Q., Newman, S., Sander, S. P., and Yung, Y. L.: Simulated

703   retrievals for the remote sensing of CO_2, CH_4, CO, and H_2O from geostationary orbit, Atmos. Meas.

704   Tech., 8, 4817–4830, https://doi.org/10.5194/amtd-8-5809-2015, 2015.

705

706   Xiong, X., Barnet, C., Maddy, E., Sweeney, C., Liu, X., Zhou, L., and Goldberg, M.: Characterization

707   and validation of methane products from the Atmospheric Infrared Sounder (AIRS), J. Geophys. Res.,

708   113, G00A01, https://doi.org/10.1029/2007JG000500, 2008.

709

710   Xiong, X., Barnet, C., Maddy, E. S., Gambacorta, A., King, T. S., and Wofsy, S. C.: Mid-upper

711   tropospheric methane retrieval from IASI and its validation, Atmos. Meas. Tech., 6, 2255–2265,

712   https://doi.org/10.5194/amt-6-2255-2013, 2013.

713

714   Yoshida, Y., Kikuchi, N., Morino, I., Uchino, O., Oshchepkov, S., Bril, A., Saeki, T., Schutgens, N.,

715   Toon, G. C., Wunch, D., Roehl, C. M., Wennberg, P. O., Griffith, D. W. T., Deutscher, N. M., Warneke,

716   T., Notholt, J., Robinson, J., Sherlock, V., Connor, B., Rettinger, M., Sussmann, R., Ahonen, P.,

717   Heikkinen, P., Kyrö, E., Mendonca, J., Strong, K., Hase, F., Dohe, S., and Yokota, T.: Improvement of

718   the retrieval algorithm for GOSAT SWIR XCO_2 and XCH_4 and their validation using TCCON data,

719   Atmos. Meas. Tech., 6, 1533–1547, https://doi.org/10.5194/amt-6-1533-2013, 2013.

720

721   Zeng, Z.-C., Zhang, Q., Natraj, V., Margolis, J. S., Shia, R. -L., Newman, S., Fu, D., Pongetti, T. J.,

722   Wong, K. W., Sander, S. P., Wennberg, P. O., and Yung, Y. L.: Aerosol scattering effects on water vapor

723   retrievals over the Los Angeles Basin, Atmos. Chem. Phys., 17, 2495–2508, https://doi.org/10.5194/acp-

724   17-2495-2017, 2017.

725

726   Zeng, Z.-C., Natraj, V., Xu, F., Pongetti, T. J., Shia, R.-L., Kort, E. A., Toon, G. C., Sander, S. P., and

727   Yung, Y. L.: Constraining aerosol vertical profile in the boundary layer using hyperspectral

728   measurements of oxygen absorption, Geophys. Res. Lett., 45, 10772–10780,

729   https://doi.org/10.1029/2018GL079286, 2018.

730

731   Zhang, Q., Natraj, V., Li, K. -F., Shia, R. -L., Fu, D., Pongetti, T. J., Sander S. P., Roehl, C. M., and

732   Yung, Y. L.: Accounting for aerosol scattering in the CLARS retrieval of column averaged CO_2 mixing

733   ratios, J. Geophys. Res., 120, 7205–7218, https://doi.org/10.1002/2015JD023499, 2015.

734

735   Zhang, Q., Shia, R. -L., Sander, S. P., and Yung, Y. L.: X_{CO2} retrieval error over deserts near critical

736   surface albedo, Earth Space Sci., 2, 1–10, https://doi.org/10.1002/2015EA000143, 2016.
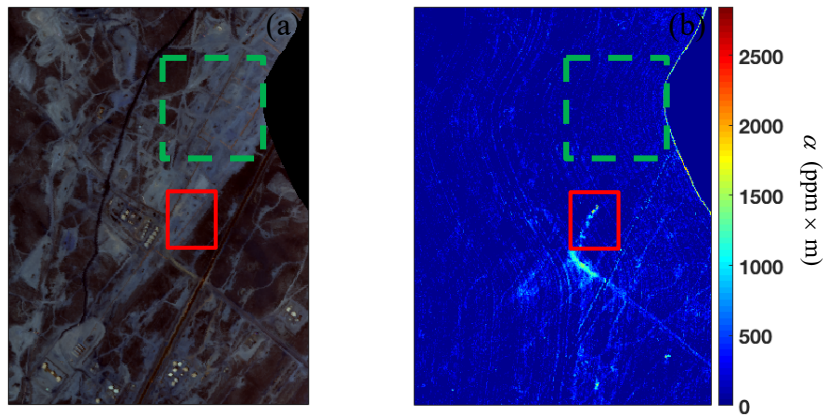
737

738

739
740
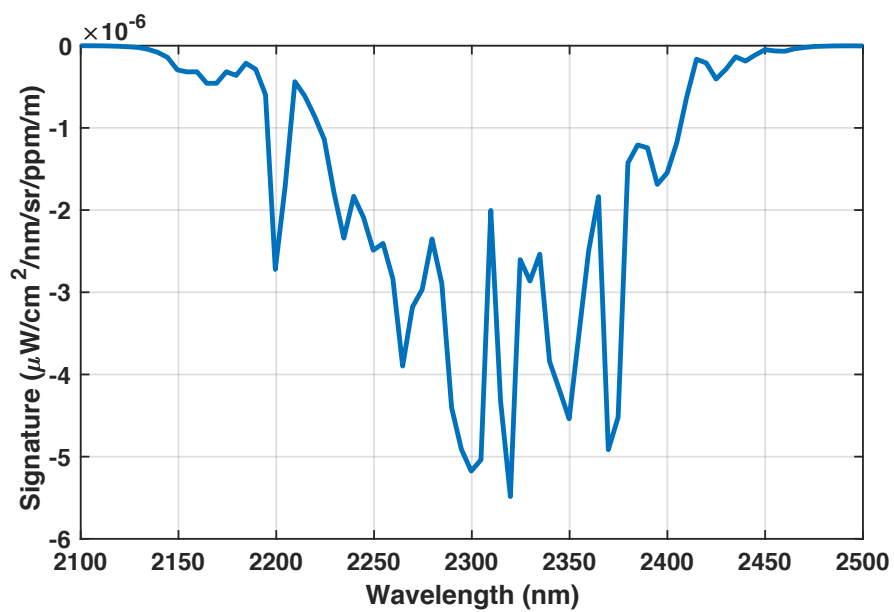
Figure 1: The target signature used for the Matched Filter method.

742

743

744

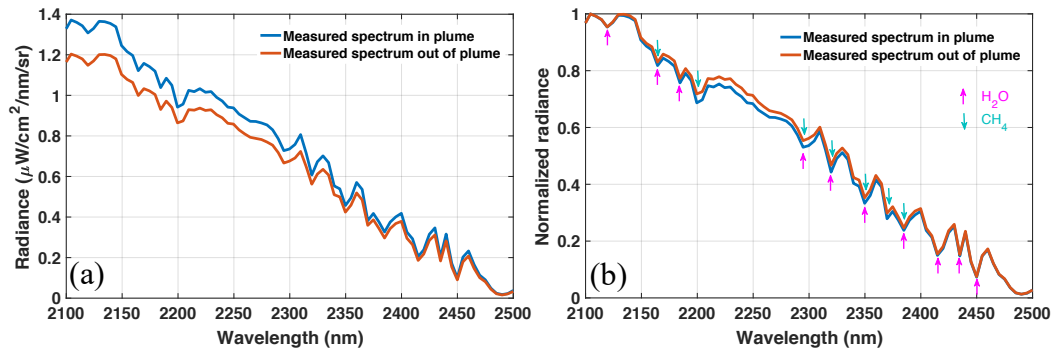745 **Figure 2: (a) RGB image of flight data from 4 September 2014 (ang20140904t204546). Adapted from**
746 **Thompson et al. (2015). (b) CH$_4$ enhancement value α (ppm × m) obtained by the MF method. An emission**
747 **source is shown in the solid red box and the background region near the target for the MF calculation is**
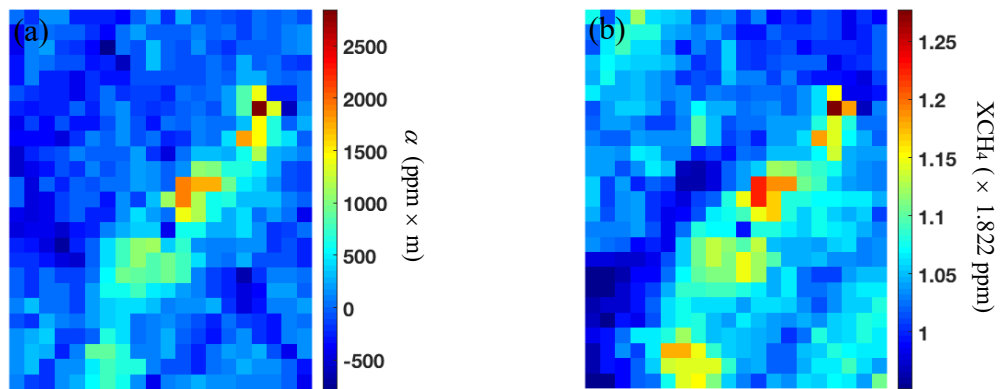748 **indicated by the dashed green box.**

749

750

751

752 **Figure 3: (a) Real radiance and (b) normalized radiance at cross-track detector elements (in and out of plume)**

753 **from the sample AVIRIS-NG measurement. The colored arrows in (b) show the main absorption features due**

754 **to H_2O (purple) and CH_4 (green).**

755

756

757

Figure 4: Retrieval image for the plume center (500 elements) based on the (a) MF method and (b) OE method.

759

760

761
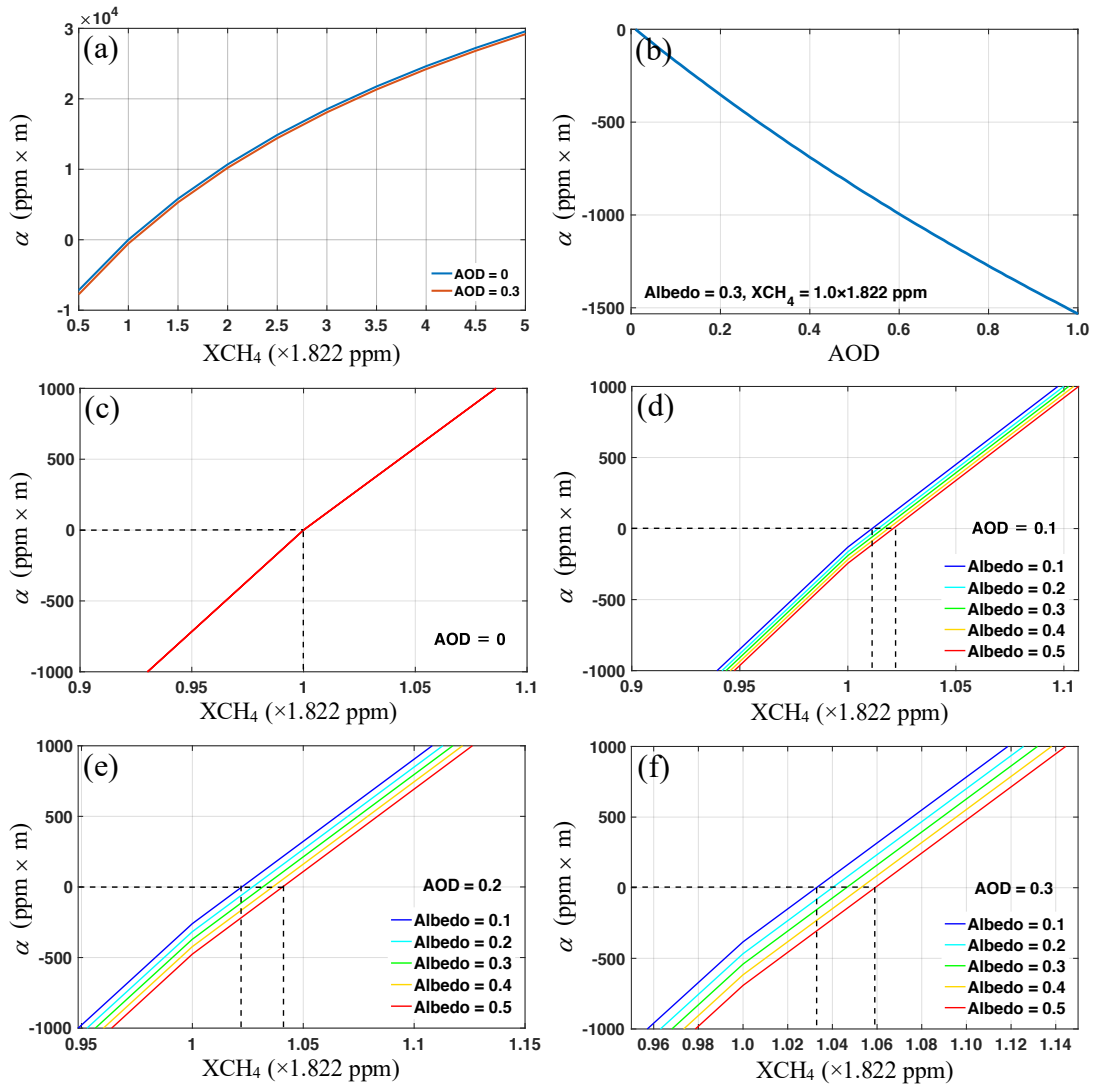
Figure 5: (a) α as a function of XCH$_4$ for AOD = 0 and AOD = 0.3 (surface albedo = 0.3). (b) α as a function of AOD (XCH$_4$ = 1.0 × 1.822 ppm, surface albedo = 0.3). Zoomed in versions of α as a function of XCH$_4$ for different surface albedos (0.1-0.5), where (c) AOD = 0, (d) AOD = 0.1, (e) AOD = 0.2, and (f) AOD = 0.3.

765

766
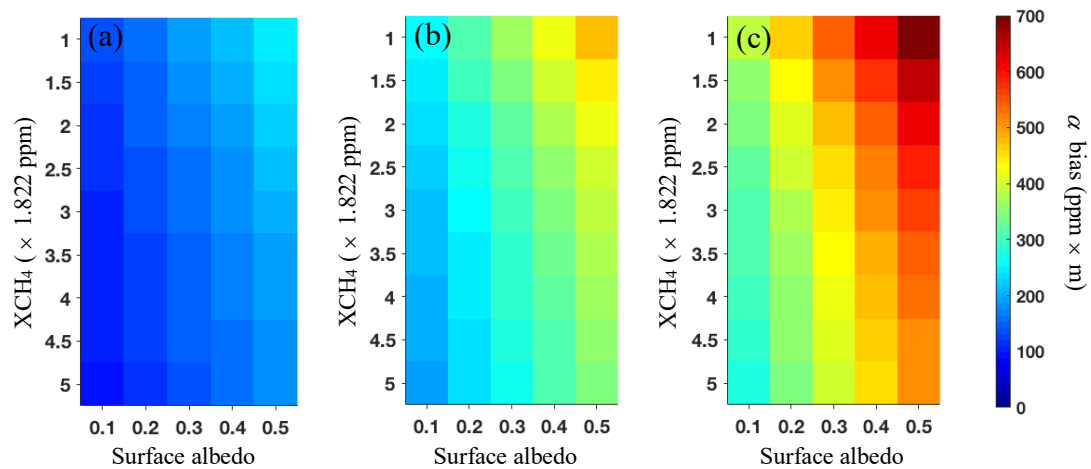
767

768   **Figure 6: Bias in α as a function of XCH$_4$ and surface albedo for (a) AOD = 0.1, (b) AOD = 0.2, and (c) AOD**
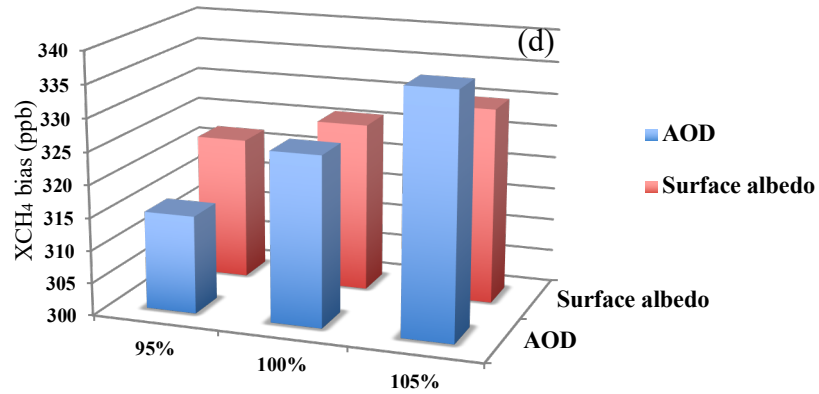
769   **= 0.3.**

770

771

772

773

774

775
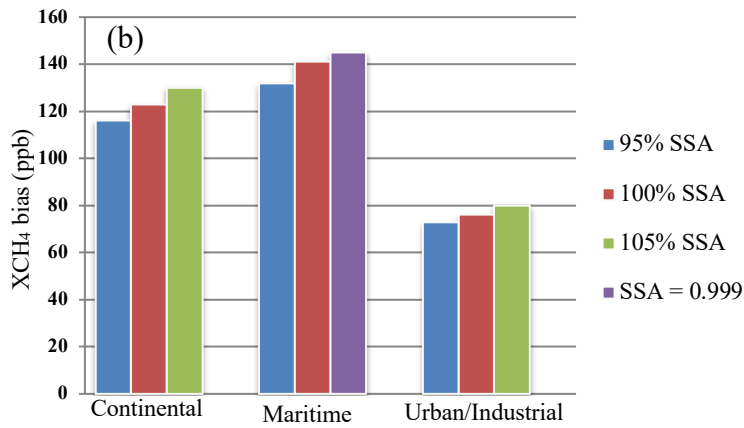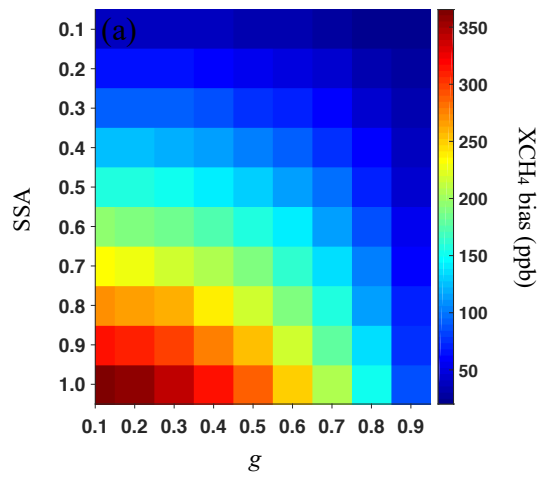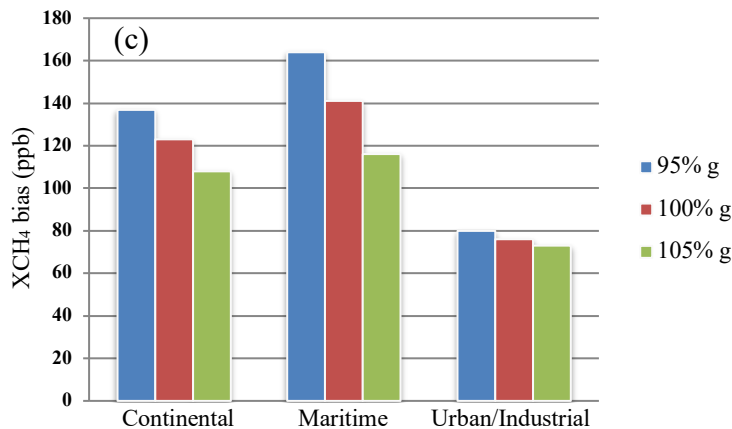
Figure 7: (a) CH₄ retrieval biases for different values of *g* and SSA. Surface albedo, AOD = 0.3, XCH₄ = 1.0

× 1.822 ppm. (b) CH₄ retrieval biases for a ± 5% change in SSA for the three aerosol mixture models. (c) Same

as (b), but for a ± 5% change in *g*.
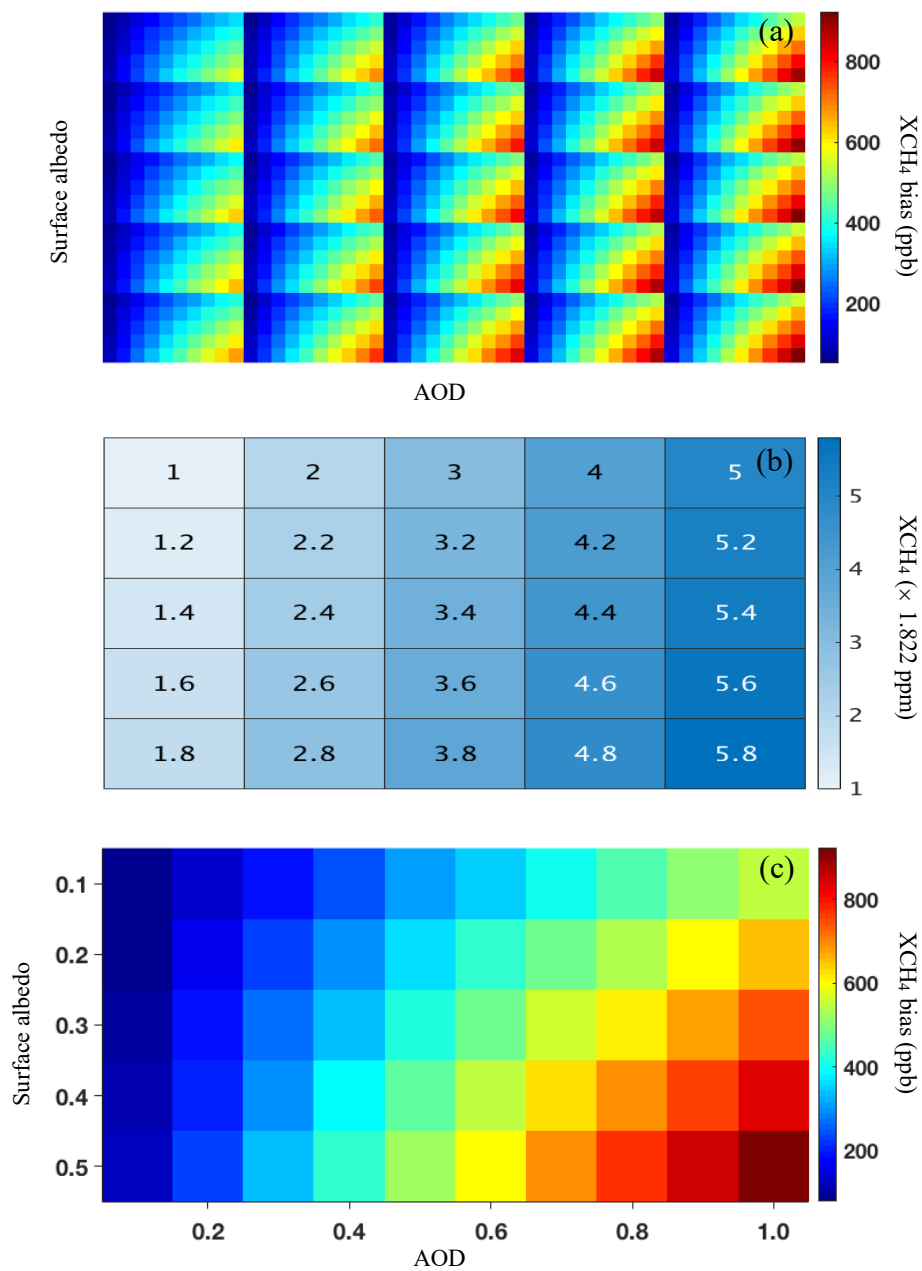
Figure 8: (a) CH$_4$ retrieval biases for different values of XCH$_4$, AOD and surface albedo. g = 0.75, SSA = 0.95. (b) XCH$_4$ for each box in (a). (c) Zoomed in plot of bottom right box (XCH$_4$ = 5.8 × 1.822 ppm). The x and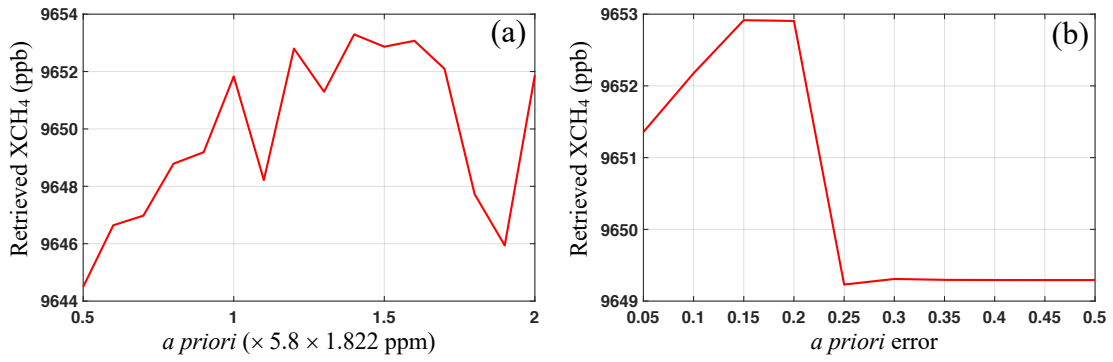 y axes show the variation of AOD and surface albedo, respectively. These changes are identical for every box in (a). (d) CH$_4$ retrieval biases for a ± 5% change in AOD and surface albedo from a base value of 0.3 (g = 0.75, SSA = 0.95, XCH$_4$ = 5.8 × 1.822 ppm).
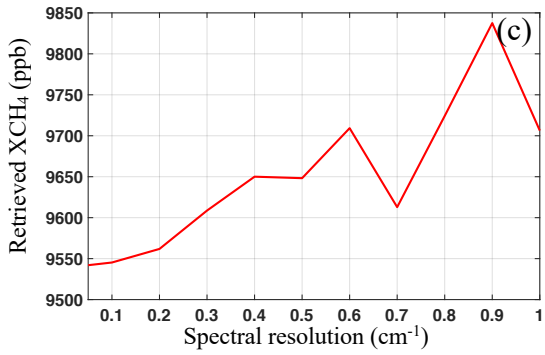
788

789

790
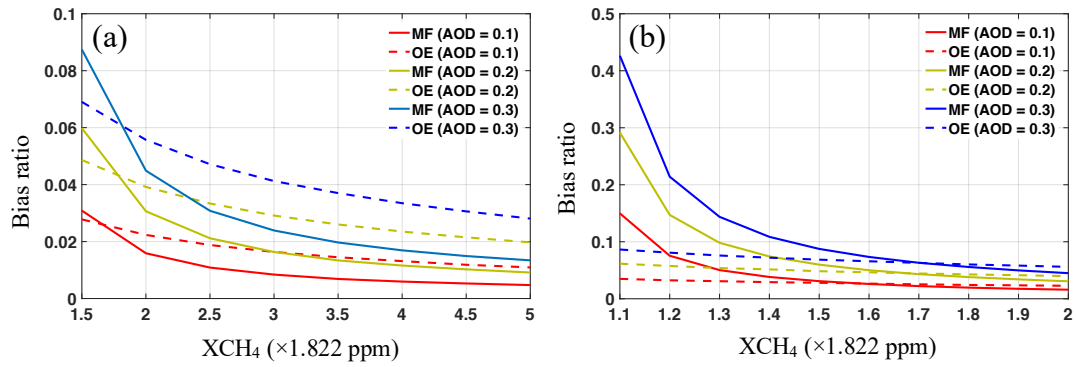

791

Figure 9: Retrieved XCH₄ for different values of (a) *a priori* **(***a priori* **error = 0.2), (b)** *a priori* **error (***a priori* **=**

5.5 × 1.822 ppm) and (c) spectral resolution. *g* **= 0.75, SSA = 0.95, AOD = 1.0, surface albedo = 0.5, XCH₄ =**

5.8 × 1.822 ppm.

795

796

797 **Figure 10: (a) Bias ratio as a function of CH$_4$ concentration for the two retrieval techniques, where the XCH$_4$**

798 **ranges from 1.5 to 5 (× 1.822 ppm). (b) Same as (a), but for XCH$_4$ ranging from 1.1 to 2 (× 1.822 ppm). Surface**

799 **albedo is set to 0.3 for all cases; results for the MF and OE methods are shown by solid and dashed lines,**

800 **respectively.**

801

802

	Dust-like	Water soluble	Oceanic	Soot
SSA	0.805	0.799	0.970	0.014
g	0.926	0.550	0.816	0.092

803   **Table 1: Optical properties of basic aerosol types (WCRP, 1986).**

804

		Continental	Maritime	Urban/Industrial
Aerosol component	Dust-like	70%		17%
	Water soluble	29%	5%	61%
	Oceanic		95%	
	Soot	1%		22%
SSA		0.746	0.966	0.314
g		0.764	0.810	0.586

805 **Table 2: Optical properties of three aerosol mixture models (WCRP, 1986).**

806

Attribute	Values
Sensor height	1 km
View zenith angle	11.91°
Solar zenith angle	30.75°
Relative azimuth angle	22.87°
Aerosol loading region	surface to 1 km
SSA	0.95
g	0.75

808   **Table 3: Inputs for the 2S-ESS model simulation.**

809